ADVANCED MATERIALS
www.advmat.de

High-Speed Fabrication of All-Inkjet-Printed Organometallic Halide Perovskite Light-Emitting Diodes on Elastic Substrates

Junyi Zhao, Li-Wei Lo, Haochuan Wan, Pengsu Mao, Zhibin Yu, and Chuan Wang**

Halide perovskites have great potential for use in high-performance light-emitting diodes (LEDs) and displays. Here, a perovskite LEDs (PeLEDs) fabricated directly on an elastomer substrate, in which every single layer in the device from bottom anode to top cathode is patterned solely using a highly scalable inkjet printing process, is reported. Compared to PeLEDs made using conventional microfabrication processes, the printing process significantly shortens the fabrication time by at least tenfold (from over 5 h to less than 25 min). The all-printed PeLEDs have a novel 4-layer structure (bottom electrode, perovskite emissive layer, buffer layer, top electrode) without separate electron or hole transporting layers. For flexible PeLEDs printed directly in ambient conditions, a turn-on voltage, maximum luminance intensity, and maximum current efficiency of 3.46 V, 10227 cd m^{-2}, and 2.01 cd A^{-1}, respectively, is achieved. The devices also exhibit excellent robustness and stability even when bent to a curvature radius of 2.5 mm. The reported device structure and fabrication processes can enable high-performance flexible PeLEDs to be manufactured over a larger area at extremely low cost and fast speed, which can facilitate the adoption of the promising PeLED technology in the emerging foldable displays, smart wearables, and many other applications.

1. Introduction

Organometal halide perovskites have sparked tremendous research interest owing to their exceptional potential for pervasive optoelectronic applications. They offer strong photoluminescence (PL) and electroluminescence (EL) emission, high carrier mobility, tunable optical bandgaps, and also superior solution processibility, which has greatly facilitated the development of high-performance light-emitting diodes (LEDs) covering the full visible spectrum.[1–7] Despite the fact that the records of quantum efficiency and device stability for perovskite LEDs (PeLEDs) have been constantly refreshed over the past decade,[8–10] there are still significant challenges related to the development of a more economical and time-efficient strategy for scalable fabrication of such devices in a flexible or stretchable form factor. If these challenges could be addressed, it could greatly benefit the application of PeLEDs in smart wearables[11] and various portable electronics with flexible or stretchable displays.

The most widely adopted procedure to obtain a perovskite functional layer is to spin coat the presynthesized perovskite solution directly onto the substrate followed by thermal annealing to evaporate the residual solvents and promote the crystallization.[2,3,12–18] Other emerging strategies including spray casting,[19,20] solution evaporation,[21] blade coating,[22,23] electrohydrodynamic printing,[4] and inkjet printing[24,25] have also been systematically studied by various research groups in recent years. Despite the fact that inkjet printing is not yet perfect, for example, requiring specially formulated printable ink, carefully tuned substrate wettability and ink rheology, and yielding relatively thick deposited film, considering the advantages of mask-free and high-resolution additive patterning, inkjet printing is still regarded as one of the most efficient alternative routes that can satisfy the requirements for potential application scenarios in next-generation flexible displays. Till now, most reported work so far claiming to adopt printing technique on perovskite displays primarily focus on the patterning of just one or two layers, usually the top electrode, on a large un-patterned perovskite film prepared by processes such as spin-coating, which result in inefficient material utilization with a significant amount of active material being wasted.[1,10,18] Additionally, these conventional coating and evaporation approaches can only demonstrate some centimeter-scale lighting panels or low-resolution patterning via time-consuming and costly stencils, which cannot satisfy the practical demand for high-resolution display panels composed of microscale lighting pixels and rapidly growing interest for customized pattern designs. By using additive manufacturing

J. Zhao, L.-W. Lo, H. Wan, C. Wang
Department of Electrical & Systems Engineering
Washington University in St. Louis
St. Louis, MO 63130, USA
E-mail: chuanwang@wustl.edu

L.-W. Lo, C. Wang
Institute of Materials Science and Engineering
Washington University in St. Louis
St. Louis, MO 63130, USA

P. Mao, Z. Yu
Department of Industrial and Manufacturing Engineering
Florida State University
Tallahassee, FL 32310, USA
E-mail: zyu@fsu.edu

The ORCID identification number(s) for the author(s) of this article can be found under https://doi.org/10.1002/adma.202102095.

DOI: 10.1002/adma.202102095

strategies such as inkjet printing, the prepared ink can be precisely deposited at the desired location with accurate volume control in picoliter-scale, indicating that it is a nearly zero-waste process and capable of the actualization of high-resolution patterning and microscale LED arrays. Moreover, the inkjet printer can be further modified based on demand for advanced and smart manufacturing. For instance, the substrate temperature during printing can be precisely controlled by using a thermoelectric heating pad to enable in situ sample annealing.

Regarding the device's flexibility, pure perovskite polycrystalline film usually consists of tightly-packed nano- or microsized crystal grains, and its large Young's modulus indicates that it can hardly survive bending or stretching.[26] Moreover, the PeLEDs are commonly constructed in a multilayer structure comprising an anode, a hole-injection layer, a light-emissive layer, an electron-injection layer, and a cathode.[12–16,27] These layers are normally deposited on an indium-tin-oxide (ITO) glass substrate followed by an evaporated or sputtered metal top electrode.[12–16] The use of such rigid substrates and brittle electrode materials also limit the mechanical flexibility of PeLEDs. To make the PeLEDs flexible or even stretchable, we have recently reported an effective approach by embedding perovskite microcrystals into a polymer matrix, where the polymer serves as an elastic connector to hold the brittle perovskite crystals together.[3] For flexible electrodes that can withstand deformation, prospective approaches include the use of sputtered metal/oxide multilayered structures,[28] eutectic indium-gallium (EInGa),[2,3] thin-films of 1D nanomaterials, such as carbon nanotubes,[29] and silver nanowires (AgNWs).[1,30–32] Among them, AgNW thin film offers high conductivity, excellent optical transparency, stretchable network structure, and can be solution-processed on flexible substrate using methods such as spin-coating,[31] spray,[33] screen printing,[1] and inkjet printing.[34] Despite the great promise, direct printing of such electrode materials on top of the perovskite film still poses great challenges because the perovskite film could be attacked by the solvents in the aforementioned conductive inks and there could also be work function mismatch. To address this issue, aliphatic amine polymer like polyethyleneimine (PEI) has been reported and used as an effective protection and buffer layer.[32,35–37]

In this work, we report the all-inkjet-printed flexible PeLEDs, in which every single layer is directly printed onto an elastomer substrate using inkjet printing. Our reported PeLEDs have a simplified 4-layer structure comprising a polyethylene oxide (PEO)-modified poly(3,4-ethylenedioxythiophene) polystyrene sulfonate (PEDOT:PSS) transparent anode, a methylammonium lead tribromide $CH_3NH_3PbBr_3$/PEO composite thin film as the light-emitting layer, a PEI buffer layer, and AgNW networks as the top cathode. We have systematically studied and optimized the rheological behaviors, viscosity, wetting, and uniformity of each type of ink in order to achieve optimal printing outcomes on elastic substrates. The mechanism of introducing an interfacial polymer layer of branched PEI to protect the perovskite crystals from being attacked and eroded by the solvents contained in AgNW ink and the effect of PEI on lowering the barrier for electron injection has also been studied. Moreover, because all printed layers are soft and deformable, the printed PeLEDs on polydimethylsiloxane (PDMS)/polyethylene terephthalate (PET) substrate exhibit good flexibility and can be repeatedly bent to a curvature radius of 2.5 mm over thousands of times without exhibiting any noticeable performance decay. Despite the fact that our PeLEDs were fabricated entirely in ambient conditions with a simple structure, outstanding performances were achieved with a turn-on voltage of 3.46 V, a maximum luminance intensity of 10 227 cd m^{-2}, and a maximum current efficiency of 2.01 cd A^{-1}. Additionally, we have managed to significantly shorten the total time it takes to complete the entire fabrication process by introducing a simplified device structure, an all-solution-based and fully-printed process, a simultaneous annealing approach, and programmed automatic trajectory control. Usually, for conventional fabrication processes, at least ≈4–5 h are necessary to fabricate one batch of microscale PeLED samples via conventional spin coating, post-treatment, and metal electrode evaporation, even without considering the time of preparing indium-tin-oxide substrates and patterning stencils. In comparison, using our process, a batch of similar PeLEDs (ten 500 × 500 μm^2 light-emissive squares) could be completed from bottom-electrode to top-electrode within 25 min. Our reported ink formulation, device structure, and printing processes could enable highly scalable and low-cost fabrication of high-performance flexible PeLEDs for a variety of applications in display and wearable electronics.

2. Results and Discussion

The fabrication processes of the all-solution-processed and fully inkjet-printed PeLEDs are schematically illustrated in **Figure 1**a. The ink formulation and fabrication process are described in detail in the Experimental Section. In brief, for the optically transparent bottom anode, a composite ink comprising the aqueous suspension of PEDOT:PSS, PEO, Triton X-100, and a small amount of ethylene glycol (EG) was used. This ink formulation offers optimal printing outcomes, good electrical property, and mechanical flexibility. The above ink was printed onto an oxygen plasma treated polydimethylsiloxane (PDMS) film spun coated on either a glass substrate or PET film, followed by an annealing process to allow the solvents to completely evaporate. The emissive layer of the PeLEDs was obtained by printing a composite ink comprising $CH_3NH_3PbBr_3$ and PEO in the 1:1 weight ratio on a heated stage at temperatures ranging from 25 to 80 °C. To protect the perovskite emissive layer from the subsequent printing steps, a PEI layer was printed on top of the $CH_3NH_3PbBr_3$/PEO composite film at elevated temperatures to allow the solvent in PEI to evaporate immediately so that only polymer PEI was left to fully cover the emissive layer. As a final step, isopropanol (IPA)-based AgNW ink with EG additive was printed along the perpendicular orientation to previously printed layers to form the top electrode. All steps were carried out in ambient conditions. Figure 1b illustrates the completed PeLED with a 4-layer structure that consists of a transparent PEDOT:PSS/PEO bottom anode, a $CH_3NH_3PbBr_3$/PEO composite emissive layer, a PEI buffer layer, and an AgNW top cathode.

Optical micrographs of representative printed PeLEDs viewed from the top AgNW cathode side and the bottom PEDOT:PSS anode side are shown in Figure 1c,d, respectively. The overlap area (500 × 500 μm^2) formed by the PEDOT:PSS/PEO bottom

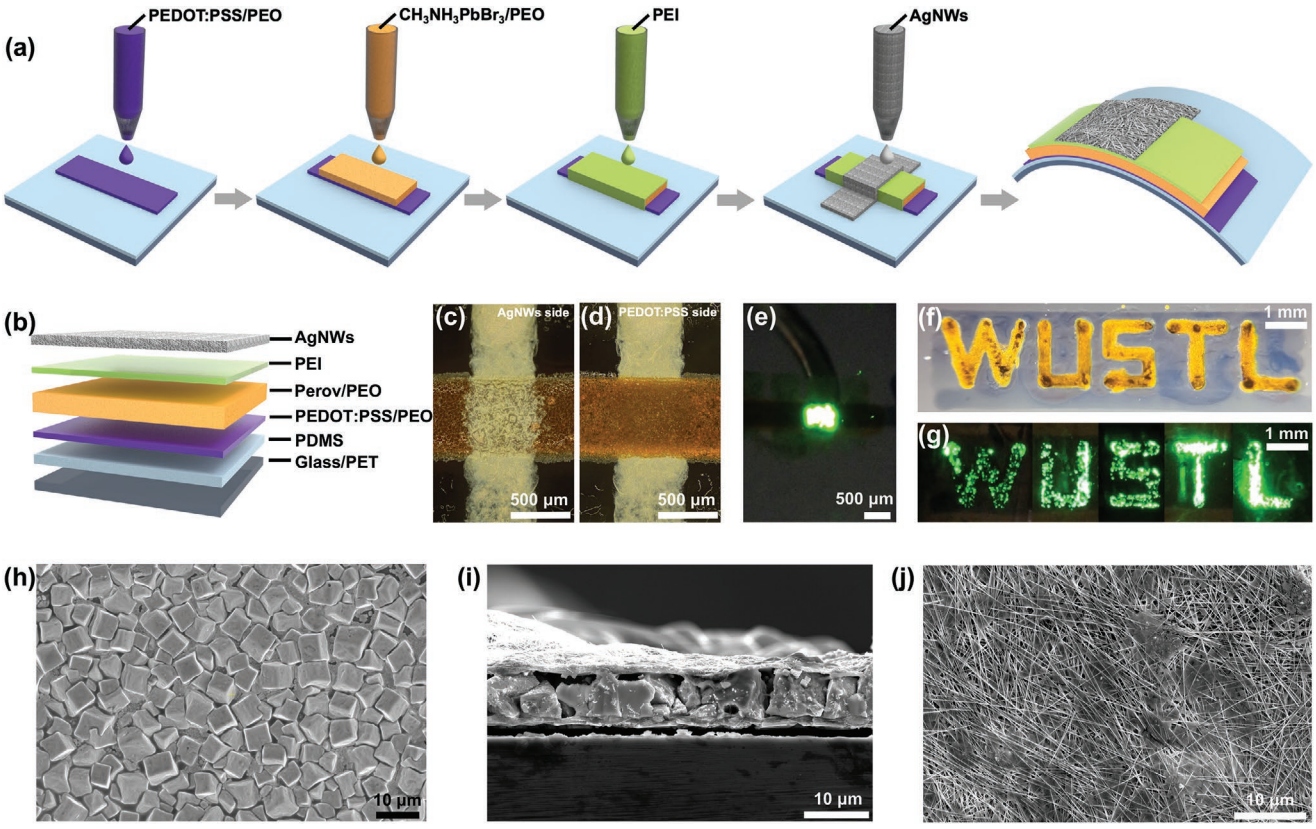

Figure 1. a) Schematic diagrams illustrating the fabrication processes of the all-inkjet-printed flexible PeLEDs. b) Printed PeLED device structure. Optical micrographs of an as-prepared PeLED on PDMS/glass substrate when viewed from the c) top AgNW cathode side and d) the bottom PEDOT:PSS/PEO anode side. e) Photograph of a lit PeLED with an applied voltage of around 4.5 V. Photographs of a printed PeLED display prototype showing "WUSTL" characters f) before and g) after being lit up with a 3.5 V bias with green light emission. h) Top view SEM image of perovskite/PEO composite (1:1) emissive layer printed onto a PEDOT:PSS/PEO film. i) Cross-sectional view SEM image of the (PEDOT:PSS/PEO)/(perovskite/PEO)/PEI/AgNWs sandwich structure printed onto a Si/SiO_2 substrate. j) Top view SEM image of the AgNW top electrode.

electrode and the AgNW top electrode is the actual light-emitting region when a bias voltage is applied. Figure 1e shows a picture of a lit PeLED emitting green light under a forward bias of 4.5 V with a measured luminance intensity of around 4200 cd m^{-2}. The printing process also allows the PeLED device to be easily patterned into arbitrary shapes. As an example, Figure 1f shows a display prototype patterned into "WUSTL" characters by programming the moving trajectory of the printing nozzle. The display can be lit up under 3.5 V with a luminance intensity of ≈1000 cd m^{-2} (Figure 1g). The quality of the luminous pattern could be further improved via increasing the flatness of the substrate as well as optimizing the nozzle-movement controlling software to generate a smoother and steadier running in the automatic printing mode. The resolution of the printed display depends on the diameter of the ink dispenser used, the viscosity of printable ink, and the wetting on the substrate. More viscous inks typically require a relatively large nozzle size to form a continuous liquid meniscus that can be dragged around smoothly. For our $CH_3NH_3PbBr_3$/PEO composite ink, under optimized printing conditions, a patterning resolution of 250 μm (Figure S1, Supporting Information) can be achieved reliably.

The surface morphology of the printed $CH_3NH_3PbBr_3$/PEO composite thin film was examined under the scanning electron microscope (SEM) as shown in Figure 1h. The $CH_3NH_3PbBr_3$ crystals (size of around ≈5–8 μm in cuboid shape) are distributed close to each other and the voids in between the grains are filled by PEO to reach a pinhole-free state. The PEO also aids the flexibility and stretchability of the perovskite film as reported in our previous work.[3] Cross-sectional SEM images were also taken from the printed PeLEDs (Figure 1i) from which the various printed layers comprising the device can be seen. On top of the PEDOT:PSS/PEO film, the polymer matrix embedded with perovskite crystals has an average film thickness that is close to the grain size in Figure 1h. The AgNW top electrode is quite conformal to the underlying $CH_3NH_3PbBr_3$/PEO emissive layer and the PEI layer is too thin to be distinguishable in Figure 1i. The top view SEM image in Figure 1j shows the dense and well-defined printed AgNW networks, which ensures low resistivity and good optoelectronic performance.

As reported in our published work, one promising pathway to make conventional perovskite emissive layer compatible with flexible electronics is to mix the perovskite precursor solution with polymer PEO, where the active components crystallize and grow in the polymer matrix during the annealing process.[2,3] In this case, the microscale perovskite crystals are embedded uniformly and tightly into the polymer binder. The polymer binder also functions as an elastomeric connector for potential

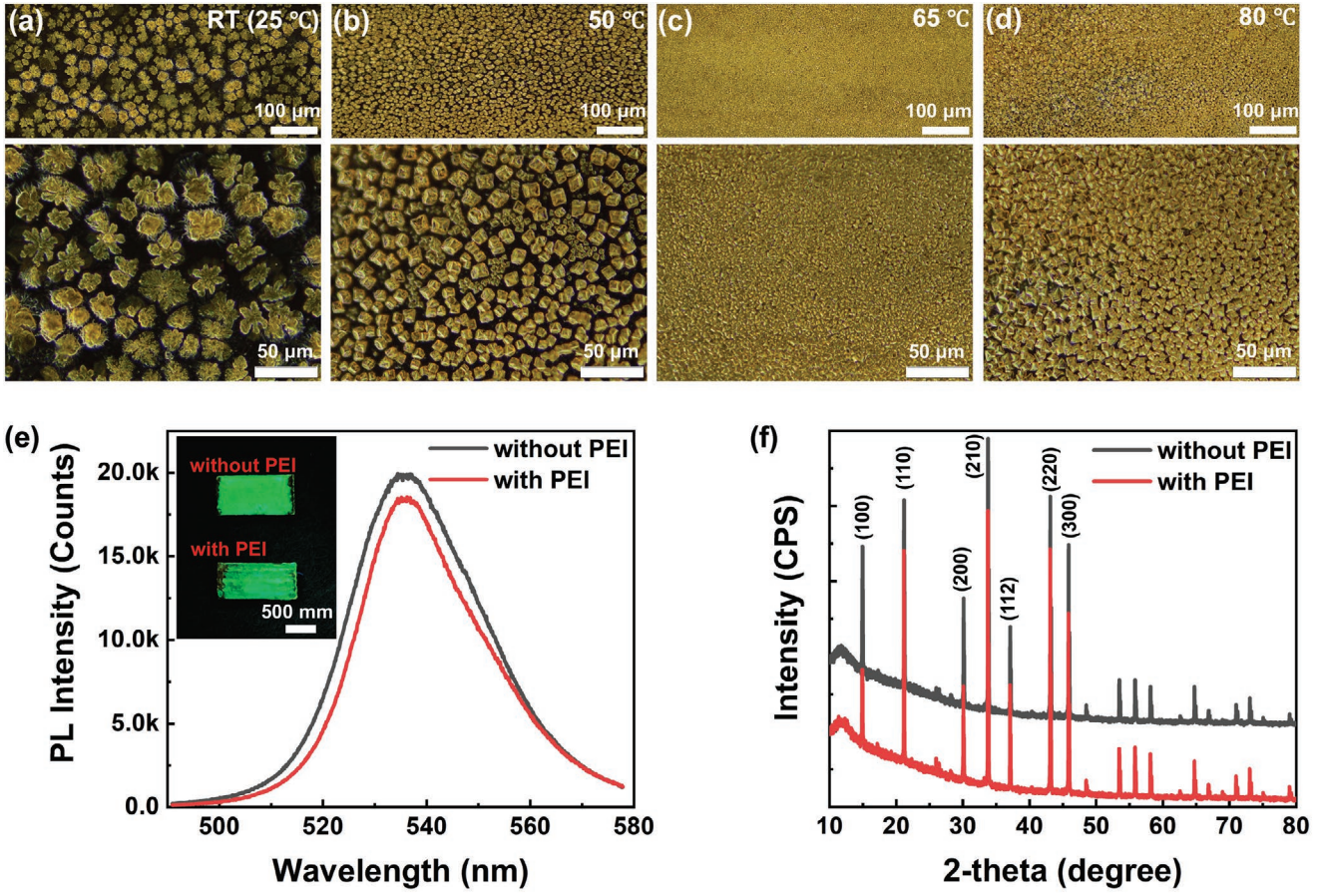

Figure 2. Characterization of the inkjet-printed $CH_3NH_3PbBr_3$/PEO composite film. a–d) Optical micrographs showing the effect of temperature on the morphology of the printed $CH_3NH_3PbBr_3$/PEO composite film. The corresponding temperatures used during printing are a) 25 °C, b) 50 °C, c) 65 °C, and d) 80 °C respectively. e) Photoluminescence spectra and f) X-ray diffraction pattern of the printed $CH_3NH_3PbBr_3$/PEO composite film (1:1) with (red trace) and without (black trace) the PEI layer, respectively. The inset in e) shows the photographs of the photoluminescence from both samples when placed under a UV light.

intrinsically stretchable PeLEDs. To form the perovskite crystals, an annealing step is needed, and it is normally performed separately after the film-forming processes such as spin-coating, drop-casting, or screen-printing. We have discovered that simultaneous annealing during the ongoing $CH_3NH_3PbBr_3$/PEO film printing process could assist the generation of perovskite nuclei by expediting the removal of residual solvent. Assisted by this on-site simultaneous annealing strategy, there is no need to adopt any further annealing post-treatment so that the manufacturing process could be significantly simplified, and the duration could be greatly shortened. This is done by placing the sample on a heating stage with the precisely controlled temperature during printing. The effect of printing temperature on the evolution of crystal size, shape, and density are presented in **Figure 2**a–d, where the top and bottom rows show the low magnification and high magnification micrographs, respectively. When printed at room temperature of around 25 °C, the $CH_3NH_3PbBr_3$ crystals form the dendritic shape with a random size of ≈20–40 µm (Figure 2a). The film is discontinuous with the grains separated by about ≈15–25 µm, leading to a poor coverage percentage of around 40%. This film discontinuity is a potentially detrimental factor in the device fabrication process since the voids between crystals can be easily penetrated by the solvents in subsequent printing inks, which will result in pinholes and current leakage or device break-down. At a higher substrate temperature of around 50 °C (Figure 2b), the perovskite precursors start to form cuboids of 10–15 µm in size, and the spacing between the crystals also shrinks significantly, resulting in a better coverage ratio of over 54%. The optimal crystal morphology is achieved at 65 °C as shown in Figure 2c, in which case the crystallized grains reach the densest arrangements with a uniform size of ≈5–8 µm. The surface coverage also peaks at 65 °C to above 90%, forming a continuous, smooth, and pinhole-free film. This printing condition is thus selected and used in the following experiments. For even higher substrate temperatures such as 80 °C (Figure 2d), the quality of the perovskite film degrades in terms of the lower coverage rate (≈70%), nonuniform crystallization, larger grain size (≈8–13 µm), and more pinhole defects. Note that all samples shown in Figure 2a–d were printed with only 2 passes (one back-and-forth round) to highlight the film morphology variation. To compare the quality of the printed film with films obtained from spin-coating (one of the most studied approaches for preparing perovskite films), a reference sample

processed by spin-coating showing the grain arrangement is provided in Figure S2 (Supporting Information). The results show that the perovskite film obtained from our ink formulation and the inkjet-printing process is quite comparable to other mainstream fabrication methods.

The optical properties of the $CH_3NH_3PbBr_3$/PEO composite film with and without PEI buffer layer were analyzed by PL spectroscopy as shown in Figure 2e. The PL intensity peaks at the same wavelength of 536 nm for both the pristine perovskite film and the one protected by the PEI buffer layer, with only a slight drop in PL intensity for the sample with PEI. The results suggest that the additional PEI protective layer has very little negative impact on the optical performance of the emissive layer. The PL spectra from the spin-coated $CH_3NH_3PbBr_3$/PEO film was also collected as a reference (Figure S3, Supporting Information), which exhibits a nearly identical peak at 534 nm. Figure 2e insets show pictures of the as-prepared $CH_3NH_3PbBr_3$/PEO composite film without (top) and with (bottom) PEI buffer layer when illuminated under UV lamp, indicating no obvious degradation in terms of color purity and luminescence intensity. The crystallinity of the pristine and PEI-protected $CH_3NH_3PbBr_3$/PEO composite film was further examined by X-ray diffraction (XRD). The samples were all prepared on top of the PEDOT:PSS/PEO bottom electrode on a PDMS substrate and thus the relative magnitudes of our XRD pattern appear slightly different from our previous results,[1–3] where the samples were fabricated on a Si/SiO_2 wafer. As shown in Figure 2f, the location and the corresponding intensity of the diffraction peaks of these two samples are highly consistent with each other, further proving that the PEI protective layer does no harm to the crystalline structure of the perovskite film.

For the top electrode, IPA-based AgNW dispersion with a concentration of 20 mg mL^{-1} was used to develop the procedure and printing recipe. The reason to choose AgNWs dispersed in IPA solvent is that IPA is one of the few solvents that have the least amount of damage to the perovskite film. **Figure 3**a shows the correlation between the AgNW sheet resistance (R_s) and the number of printing passes. As the number of printing passes increases from 5 to 40, the R_s decreases drastically from 6900 to 2.2 Ω sq^{-1}. A good tradeoff happens at around 10 printing passes with an acceptably low R_s of 55.2 Ω sq^{-1} and reasonable time consumption (less than 30 s), and it is thus selected as the optimal number of printing passes for the following experiments unless otherwise noted. However, one problem with IPA-based ink is that it exhibits excellent wettability on a polymer substrate, which means that the ink can easily bleed broadly, and it makes it challenging for achieving precise microscale patterning. To solve the above problem, EG was added to tune the rheology and wetting property of the AgNW ink.[30,34] Figure 3b exhibits that sheet resistance increases drastically from 55 Ω sq^{-1} to 3.6 MΩ sq^{-1} as the EG volume ratio increases from 0 to 50 vol%, which can be attributed to the diluted concentration of conductive nanowires. On the other hand, the contact angle between the AgNWs/IPA/EG mixed ink droplet and substrate underwent a gradual increase from 27.7° to 67.1°, indicating that the wettability of the ink was lowered by the introduction of EG, which is promising for achieving high-resolution printing. The morphology of printed AgNW networks using different formulas is compared in Figure 3c–h with the insets showing the zoomed-in view of the film. For the AgNW networks printed with pure IPA-based AgNW ink without EG additive (Figure 3c), it is obvious that the nanowires are pulled toward the edges due to the coffee-ring effect caused by the fast evaporation of solvent IPA. Such nonuniform nanowire networks may result in poor coverage of printed top electrodes and local breakdown of the PeLED device. The addition of EG plays a crucial role to tune the rheology of ink[30] and reduce the possibilities of nozzle clogging by contributing to a more stable and uniform AgNW dispersion.[34] With an increasing EG volume ratio, the coffee-ring effect is practically eliminated. Only a few nanowire aggregations can be observed in ink with 10 vol% EG (Figure 3d), which totally vanished in inks with even higher EG concentration (Figure 3e–h). Nevertheless, the added EG also results in a decrease in AgNW networks density and the corresponding degradation of electrical conductance in Figure 3b. For the sample with 50% EG shown in Figure 3h, the nanowire density is too low to form percolating networks and the film is almost not conductive. The effect of the EG additive on the wettability of the mixed AgNW ink is also illustrated in Figure 3i, in which the width of the printed features (with 2 printing passes) shrank from 677 to 389 μm with increasing EG ratio, suggesting that the ink seepage issue was better controlled. Considering all the factors mentioned above, the optimal AgNW ink formula was chosen to be 80 vol% IPA-based AgNWs with 20 vol% EG. The printed samples from such ink exhibit a sheet resistance of 220 Ω sq^{-1} and reasonable capability for precise printing.

The underlying mechanism behind the use of EG to tune the ink drying behavior and enhance the quality of deposited AgNW networks can be attributed to EG's high boiling point (197 °C) and high viscosity. It is known that the coffee ring effect is mainly due to the faster evaporation along the edge interfacial line, which induces a continuous compensate flow carrying the solute (AgNWs in this case) from the center to the pinned contact line.[38] What's worse, because the sample was placed on a heating pad to expedite the annealing process during printing, the elevated temperature will speed up the outward replenishing flow and strengthen the coffee ring effect.[39] By adding EG, the increase in boiling point will slow down the unbalanced evaporation rate difference between the central and edge regions. Meanwhile, the increased ink viscosity will also suppress the tendency of nanowires migrating toward the marginal interface.[40]

For the printed PEDOT:PSS/PEO bottom electrode, we have adopted the recipe from our recent publication with a PEO blending ratio of 35 vol%, which is printing-friendly and also offers intrinsic stretchability.[3,41] The optical transmittance of the printed PEDOT:PSS/PEO composite film with a various number of printing passes was characterized using ultraviolet–visible spectroscopy (UV–Vis) and the results are shown in Figure 3j. At a wavelength of 535 nm, the measured transmittance of the film decreases slightly from 91% to 81% as the printing passes increase from 5 to 20, followed by a considerable drop to 63% at 30 printing passes. The inset picture of Figure 3j shows the visual difference of the printed PEDOT:PSS/PEO films with different numbers of printing passes. On the other hand, with increasing printing passes, the thickness of

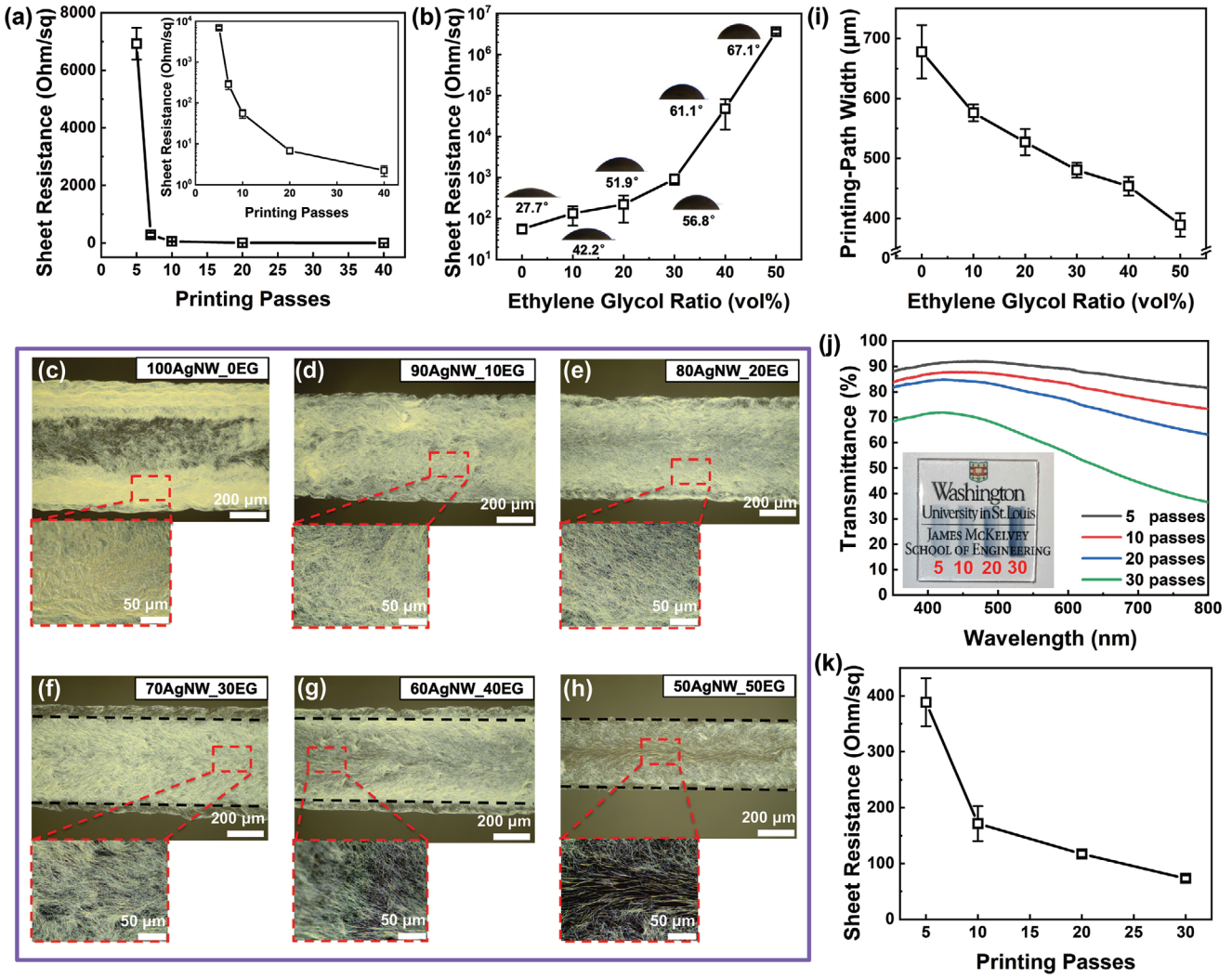

Figure 3. Characterization of the printed AgNW top cathode and PEDOT:PSS/PEO composite bottom anode. a) Sheet resistance of the printed AgNW thin-film as a function of the number of printing passes. Inset: Same data presented in semilogarithm scale. b) Sheet resistance of the AgNW networks printed on PEI/PDMS substrate (10 printing passes) as a function of EG additive in the AgNW dispersion. Insets: Micrographs showing the evolution of contact angles between the AgNWs/EG mixed ink droplet and substrate with increasing EG volume ratio. c–h) Micrographs showing the surface morphology of the printed AgNW networks (2 printing passes) using inks with various additive volume ratio. Inset: zoom-in view of AgNW networks. i) Path width of printed AgNW pattern as a function of EG additive volume ratio. j) Transmittance of the PEDOT:PSS-PEO composite film with different numbers of printing passes. Inset: Photograph showing the visual difference in transparency of the film with 5, 10, 20, and 30 passes, respectively. k) Sheet resistance of the printed PEDOT:PSS/PEO composite film as a function of number of printing passes.

the PEDOT:PSS/PEO film increases so that the film conductance also improves noticeably. More specifically, the sheet resistance of the PEDOT:PSS/PEO composite electrode drops from 389 Ω sq^{-1} at 5 printing passes to 73 Ω sq^{-1} at 30 printing passes (Figure 3k). As a tradeoff, we have selected 20 printing passes as the optimal recipe, which offers high optical transparency of 81% at 535 nm wavelength and low sheet resistance of 117 Ω sq^{-1}, which is comparable to rigid transparent electrode counterparts such as sputtered ITO.

The performances of PeLEDs including current density–voltage (*J*–*V*), luminance–voltage (*L*–*V*), and current efficiency–voltage (*CE*–*V*) characteristics were measured and the results are presented in **Figure 4**a–c. As discussed above, a PEI buffer layer was printed on top of the $CH_3NH_3PbBr_3$/PEO emissive layer before the printing of the AgNW cathode. This PEI interfacial layer protects the perovskite emissive film from being attacked by the solvent in the AgNW ink during the top electrode printing step, which results in improved device yield. However, it is worth noting that because the branched PEI is an insulating polymer, it could certainly weaken the carrier transport, and thus a tradeoff must be made between the device yield and device performance. The thickness of the PEI buffer layer can be tuned by varying the concentration of the PEI solution. Aimed at finding the concentration of PEI solution that offers the best device performance, we have prepared and compared PeLED devices without and with 10, 20, and 40 mg mL^{-1} of PEI printed on top of the $CH_3NH_3PbBr_3$/PEO composite film.

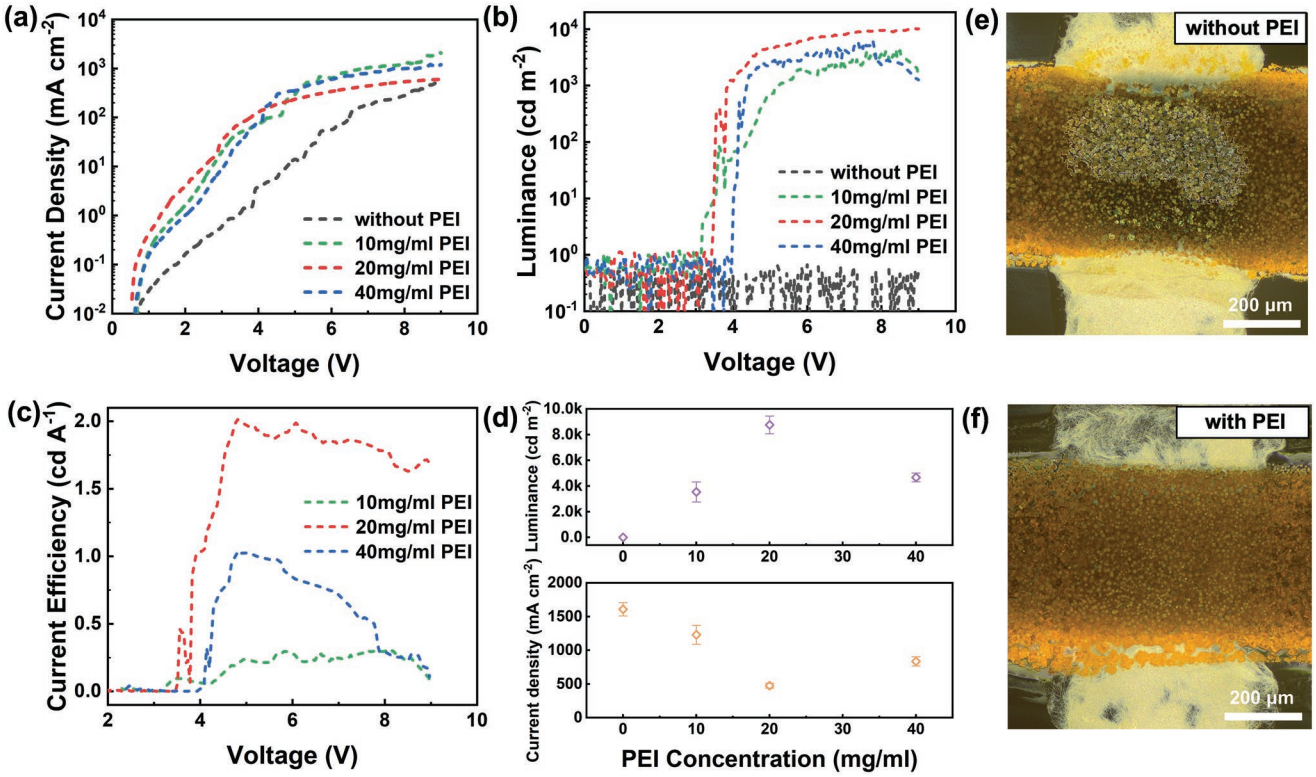

Figure 4. Optoelectronic characteristics of the all-inkjet-printed $CH_3NH_3PbBr_3$ PeLEDs. a) Current density, b) luminance, and c) current efficiency versus voltage characteristics of the fully printed PeLEDs with printed PEI buffer layer of different concentrations. d) Plot showing luminance and current density versus PEI concentration with a 7 V bias voltage. e,f) Optical micrographs of the as-prepared PeLED without and with the additional PEI protective layer when viewed from the bottom PEDOT:PSS/PEO anode side. The images clearly show that the PEI layer is effective in protecting the perovskite film from being dissolved during the AgNW printing process.

As shown in Figure 4a, the *J*–*V* curves all exhibit the as expected exponential relationship with bias voltage and a maximum current density J_{max} of 473, 2100, 601, and 1232 mA cm^{-2} (measured at 9 V) are achieved in PeLEDs without and with 10, 20, 40 mg mL^{-1} PEI, respectively. The decrease of J_{max} for increasing PEI concentration from 10 to 20 mg mL^{-1} can be attributed to the insulating nature of PEI, while the inconspicuous rise for the sample with 40 mg mL^{-1} PEI could be explained by the nonuniform PEI film coverage caused by the printing of extremely high-viscosity PEI solution. Compared with the flat PEI capping layer with a uniform thickness in Figure 1i, the content of PEI in 40 mg mL^{-1} solution is remarkably high so that it gets too viscous to be carried by the solvent for uniform coverage. As a result, the PEI content may accumulate in valleys among perovskite crystals, resulting in some regions being thicker (red-circled regions in Figure S4a, Supporting Information) and some other regions being thinner (blue-circled regions in Figure S4a, Supporting Information) to allow more current to pass through. The nonuniform PEI buffer layer can potentially result in defective or even dead pixels on lit PeLEDs (Figure S4b, Supporting Information).

As shown in Figure 4b, the device without the PEI buffer layer could not be lit up due to damage to the emissive layer caused by the AgNW printing process. In contrast, the PeLED with PEI buffer layer exhibit turn-on voltages (defined as the voltage applied with luminance intensity of 1 cd m^{-2}) of 3.18, 3.46, and 4.02 V and a maximum luminance intensity L_{max} of 4325, 10 227, and 6239 cd m^{-2}, respectively. The gradual increase in turn-on voltage with a higher PEI mass fraction also corresponds to the PEI's insulating nature. For all devices, the luminance intensity increases abruptly between 3 and 4 V and reaches a relatively flat plateau after around 5 V. For the *CE*–*V* curves shown in Figure 4c, the three types of PeLEDs with 10, 20, and 40 mg mL^{-1} PEI exhibit maximum current efficiency CE_{max} of 0.32 cd A^{-1} (at 8.12 V), 2.01 cd A^{-1} (at 4.82 V), and 1.04 cd A^{-1} (at 4.83 V), respectively, and the corresponding external quantum efficiency (*EQE*) is calculated to be 0.128% (4070 cd m^{-2}), 0.804% (4362 cd m^{-2}), and 0.416% (2566 cd m^{-2}), respectively. Figure 4d summarizes the luminance and current density of the PeLEDs as a function of the PEI concentration used for printing the buffer layer. The results indicate that the 20 mg mL^{-1} PEI offers the highest luminance of 8754 cd m^{-2} but the lowest current density of 474 mA cm^{-2}. Note that all data in Figure 4d were measured at 7 V bias voltage. Overall, the achieved performances such as low turn-on voltage, high luminance, and efficiency are among the best compared to previously reported flexible PeLEDs adopting $MAPbBr_3$ polycrystalline films as the emissive layer (Table S1, Supporting Information).

It is well-known that perovskite is particularly sensitive to oxygen, moisture, and many common solvents, which explains why AgNW ink cannot be printed directly on top of

the perovskite film. The role of the PEI interfacial layer is to physically protect the $CH_3NH_3PbBr_3$/PEO emissive layer from attacks by multiple solvents (IPA and EG) in the AgNW ink during the top electrode printing step. The micrographs in Figure 4e,f show the PeLEDs without and with PEI interlayer when viewed from PEDOT:PSS/PEO bottom electrode side. It is obvious that the appearances of these two samples are drastically different. For the sample without PEI protection in Figure 4e, the perovskite film is corroded significantly by the AgNW ink, and the $CH_3NH_3PbBr_3$ crystals degraded severely with an obvious color change from orange to gray. In contrast, the other sample with PEI protection in Figure 4f was well-protected without any visible corrosion based on the morphology of $CH_3NH_3PbBr_3$ crystals. Electrical tests on these two samples also confirmed that the top one without PEI buffer layer failed, while the bottom one with PEI could work well with bright light emission. In order to determine which component in the AgNW ink does the most harm to the underlying perovskite functional layer, a control experiment was carried out by printing pure IPA (Figure S5a, Supporting Information) and pure EG (Figure S5b, Supporting Information) onto the $CH_3NH_3PbBr_3$/PEO layer without (top row) and with (bottom row) PEI buffer layer. The results indicate that IPA did little harm to the perovskite emissive layer, while EG results in catastrophic degradation to the perovskite crystals (upper right picture in Figure S5b, Supporting Information) as indicated by the color change which also matches the results in Figure 4e. With the help of the PEI protective layer, the erosion from EG could be mitigated (bottom right picture in Figure S5b, Supporting Information). To further support that the PEI buffer layer could effectively protect the perovskite active layer from being eroded by EG, XRD patterns and photoluminescence were measured from the samples with and without PEI protection and the results confirm that the PEI plays a key role in protecting the sensitive perovskite material from chemical attacks (Figure S6, Supporting Information).

In addition, it is worth pointing out that PEI interfacial layer may also be regarded as an electrode work function modifier,[32,36] which could facilitate the electron injection by effectively suppressing the injection barrier. Furthermore, as the perovskite freely crystalized during the annealing process, the outermost surface of the $CH_3NH_3PbBr_3$/PEO composite film is still not perfectly smooth even though most pinholes have already been filled by the PEO. As shown in Figure 1i; and Figure S4a (Supporting Information), the PEI could also help planarize and smooth the surface defects by serving as a capping agent to fill the concaves and valleys among crystals. This PEI buffer layer may also enhance the interfacial adhesion by serving as a binder between the perovskite layer and AgNW networks, which leads to a more compacted AgNW top electrode with reduced contact resistance.[42] The improved adhesion can be further confirmed by peel tests (Figure S7, Supporting Information), which show that for the sample with a PEI buffer layer, the printed top AgNW electrode is denser and remain bonded to the functional layer underneath even after an adhesive tape is used.

The mechanical flexibility and durability of PeLEDs were also characterized. The devices were printed on top of a PDMS substrate with a flexible polyethylene terephthalate (PET) support. Because each layer in the printed PeLEDs is intrinsically stretchable to some extent, the device has the capability to withstand significant deformation. The current density and luminance of the device at a 3.5 mm curvature radius were examined before and after 10 or 100 cycles. As shown in **Figure 5**a, the three *J*–*V* curves nearly all overlapped with each other without exhibiting any noticeable differences after 100 cycles. The *L*–*V* curves in Figure 5b also demonstrate a high degree of consistency with only a slight drop in luminance intensity from 8885 cd m^{-2} (fresh device) to 8250 cd m^{-2} (after 100 bending cycles) at 9.0 V. As shown in Figure 5c, when bent down to a concave shape with a 3.5 mm radius, the PeLED remained lit and kept emitting stable green light. By inspecting the surface morphology of the perovskite functional layer under various bending radii, we can conclude that the bending limit is a curvature radius of around 2.5 mm (Figure S8c, Supporting Information). Under such bending condition, the tensile strain induced in the actual device is estimated to be around 7% (Figure S9, Supporting Information). We have further tested the durability of the flexible PeLED with up to 5000 bending cycles. The normalized luminance only dropped by 5.5% and the corresponding current efficiency decreased by less than 15% (Figure 5d), which further confirm that a curvature radius of 2.5 mm is a safe limit for the device. The demonstrated mechanical robustness under such strain level exceeds most of the previously reported flexible PeLEDs (Table S1, Supporting Information).

Finally, a long-term aging test was conducted to study the stability of the printed PeLEDs. Usually, the perovskite material degrades quickly in the air due to its sensitivity to oxygen and moisture, which is the main reason why perovskite optoelectronic devices are normally fabricated and stored inside glove box with the protection from inert gases. In our case, because the active layer is polycrystalline perovskite filled by polymer binder in the voids, it is more difficult for the oxygen and moisture to penetrate into the emissive layer and therefore the degradation can be significantly slowed down. As shown in Figure S10 (Supporting Information), the normalized luminance and current density of our all-inkjet-printed PeLEDs only experienced slight drops of around 9.2% and 6.6%, respectively, after the sample was exposed in ambient air (temperature 25 °C, humidity 40%) for 100 h. Meanwhile, the normalized current efficiency stayed nearly the same as the initial value without obvious decay.

3. Conclusion

In summary, we have reported a flexible halide perovskite LED fabricated entirely by highly efficient inkjet printing processes on elastic substrates. The device has a simple 4-layer sandwich structure with a PEDOT:PSS/PEO transparent bottom electrode, a $CH_3NH_3PbBr_3$/PEO composite emissive layer, a PEI buffer layer, and an AgNW top electrode. We have systematically studied and optimized the ink formulation for optimal printing outcomes. Moreover, by employing a PEI buffer layer in between the perovskite film and the top electrode, the perovskite emissive layer can be effectively protected from the solvents in subsequent printing steps, which helps improve device yield and performance. The PeLEDs with optimized printing

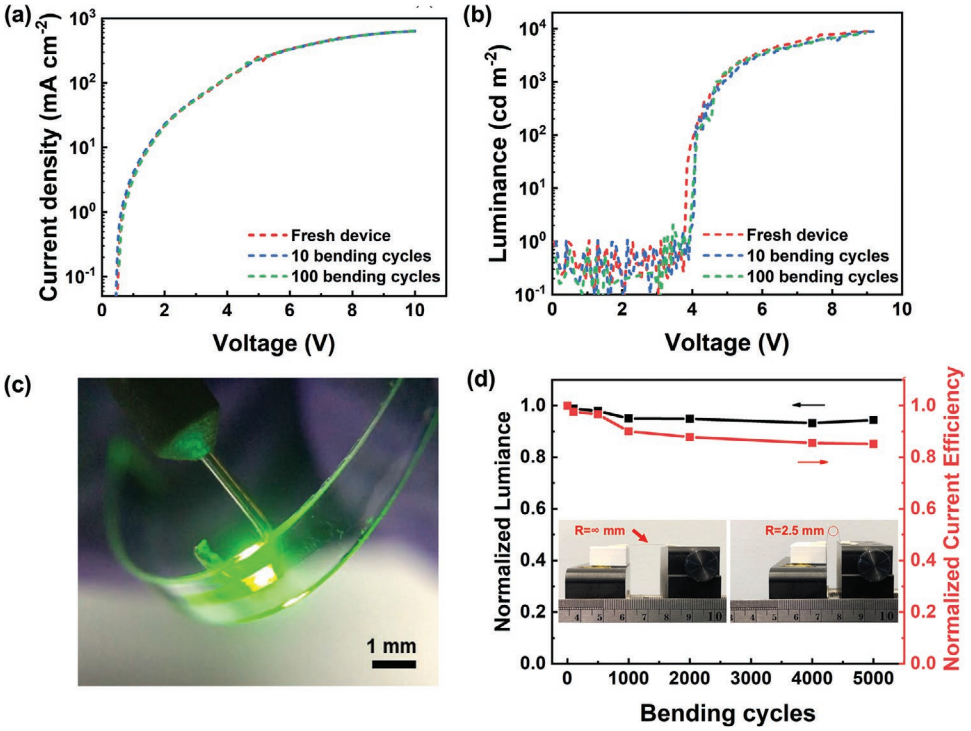

Figure 5. Bending tests conducted on the fully inkjet-printed flexible PeLEDs. a) Current density and b) Luminance versus voltage characteristics of the flexible PeLEDs before and after being bent for up to 100 cycles, respectively. c) A PeLED fabricated on a flexible PDMS substrate when being lit and bent to a curvature radius of 3.5 mm. d) Normalized luminance and current efficiency measured after 5000 bending cycles with a curvature radius of 2.5 mm. The insets show the experimental setup for the bending test at pristine and bending states.

recipe exhibit a low turn-on voltage of 3.46 V, a maximum brightness of 10 227 cd m^{-2}, a favorable current efficiency of 2.01 cd A^{-1}, and are robust to bending cycles without any noticeable performance degradation. These key performance metrics are largely competitive or even superior to other reported flexible PeLEDs. The ink formulations and fabrication strategies proposed in this paper may pave a promising way for low-cost and scalable manufacturing of perovskite optoelectronic devices for emerging applications.

4. Experimental Section

Materials: Lead (II) bromide ($PbBr_2$, 99.999%), poly(ethylene oxide) (PEO, average M_v ≈5 000 000), *N*,*N*-dimethylformamide (DMF, 99.8%), dimethyl sulfoxide (DMSO, >99.9%), branched polyethylenimine (PEI, average M_w ≈25 000 by LS, average M_n ≈10 000 by GPC), Triton X-100, ethylene glycol, and poly(3,4-ethylenedioxythiophene)-poly(styrene sulfonate) (PEDOT:PSS, 1.1% in H_2O) were purchased from Sigma-Aldrich. Methylammonium bromide (CH_3NH_3Br) and Sylgard 184 kit (Silicone elastomer base and curing agent) were purchased from "1-Material Inc" and Dow Silicones Corporation, respectively. IPA-based silver nanowire dispersion (D:90 nm, L:20–30 µm) was purchased from ACS Material, LLC.

Ink Formulations: The PEDOT:PSS precursor was prepared by mixing aqueous PEDOT:PSS, ethylene glycol, and Triton X-100 with a volume ratio of 100: 5: 1. The PEO solution was obtained by dissolving PEO in DMF with a concentration of 10 mg mL^{-1} followed by stirring at 60 °C. The PEDOT:PSS precursor and PEO solution were then mixed with a weight ratio of 100: 35 to obtain the PEDOT:PSS/PEO composite ink, which was stirred at 500 rpm for 30 min before use. The $CH_3NH_3PbBr_3$ perovskite ink was prepared by mixing the precursors of $PbBr_2$ and CH_3NH_3Br with a molar ratio of 1:1.5 and then dissolve in anhydrous DMSO to reach a concentration of 500 mg mL^{-1}. The $CH_3NH_3PbBr_3$ suspension was stirred at 70 °C for 20 min to expedite the dissolution until the white sediment totally disappeared. The $CH_3NH_3PbBr_3$/PEO composite ink was obtained by mixing the $CH_3NH_3PbBr_3$ precursor and the PEO solution with a weight ratio of 1:1. Fresh ink should be made before each experiment and stirred at 70 °C for 30 min. The PEI ink was prepared by dissolving the branched PEI into IPA at the desired weight ratio. The AgNW ink consists of as-purchased IPA-based AgNW dispersion and EG that were mixed to the desired volume ratio. Before each use, the AgNW ink was sonicated for 2 min to eliminate the entangled nanowire aggregations, which is essential to avoid nozzle clogging and achieve more uniform printing.

Flexible PeLED Fabrication: The entire fabrication process was carried out in ambient conditions with a humidity of around 40%. The Microplotter (Sonoplot Inc.) was modified with a thermoelectric heating pad and a temperature controller (TE Technology Inc.) to allow precise temperature control of the sample during the printing. The PDMS elastomer base and curing agent were mixed at a mass ratio of 10:1, followed by vacuum treatment to remove the air bubbles. The PDMS substrate was prepared by casting the as-prepared PDMS onto a glass or PET substrate that was cleaned by IPA and deionized water. Right before printing, the PDMS substrate was treated by oxygen plasma (Plasma Etch PE25-JW-HF) at 30 W for 15 s. The as-prepared PEDOT:PSS/PEO composite ink was then loaded into the ink dispenser of the microplotter, which was gradually lowered to establish a quasicontact with the PDMS surface to form an ink meniscus. Predesigned patterns were printed with the ink dispenser moving at a rate of 2000 µm s^{-1}. After printing, the PEDOT:PSS/PEO film was annealed on-site at 90 °C to completely remove the solvents. Following similar steps, the $CH_3NH_3PbBr_3$/PEO composite ink was printed on top of the PEDOT:PSS/PEO bottom electrode with a speed of 1000 µm s^{-1} with simultaneous annealing at the desired temperature ranging from 25 °C (room temperature) to 80 °C. PEI buffer layer was subsequently printed on top of the annealed

perovskite composite film at a speed of 1000 μm s^{-1}. This printing step was conducted at 80 °C to evaporate IPA solvent immediately. As the last step, the AgNW top electrodes were printed with the substrate maintained at 90 °C during printing for the same reason described above.

PeLED Measurement: The current density–voltage (*J–V*) and luminance–voltage (*L–V*) relationships were characterized on a homemade measurement setup, which is constructed with one three-axis manual stage holding the sample, one *z*-axis linear stage holding a metal probe for applying voltage, a silicon photodiode used to capture the light emission, and some other optomechanical components purchased from ThorLabs. The PeLED device current and photodiode photocurrent were measured using a semiconductor device analyzer (Keysight B1500A). For bending tests, the sample was mounted onto a syringe pump whose motion cycles could be precisely controlled. The flat state and the bending state with desired curvature radius were set by adjusting the initial and ending positions of the syringe pump.

Supporting Information

Supporting Information is available from the Wiley Online Library or from the author.

Acknowledgements

This work was funded by Washington University. The authors acknowledge the Institute of Materials Science and Engineering at Washington University for the use of instruments and staff assistance.

Conflict of Interest

The authors declare no conflict of interest.

Data Availability Statement

The data that support the findings of this study are available from the corresponding author upon reasonable request.

Keywords

flexible electronics, inkjet printing, light-emitting diodes, perovskites, solution process

Received: March 17, 2021
Revised: August 20, 2021
Published online: October 8, 2021

[1] S. G. Bade, J. Li, X. Shan, Y. Ling, Y. Tian, T. Dilbeck, T. Besara, T. Geske, H. Gao, B. Ma, K. Hanson, T. Siegrist, C. Xu, Z. Yu, *ACS Nano* **2016**, *10*, 1795.
[2] J. Li, S. G. Bade, X. Shan, Z. Yu, *Adv. Mater.* **2015**, *27*, 5196.
[3] S. G. R. Bade, X. Shan, P. T. Hoang, J. Li, T. Geske, L. Cai, Q. Pei, C. Wang, Z. Yu, *Adv. Mater.* **2017**, 29.
[4] M. Zhu, Y. Duan, N. Liu, H. Li, J. Li, P. Du, Z. Tan, G. Niu, L. Gao, Y. Huang, Z. Yin, J. Tang, *Adv. Funct. Mater.* **2019**, *29*, 1903294.
[5] F. Zhang, H. Zhong, C. Chen, X.-g. Wu, X. Hu, H. Huang, J. Han, B. Zou, Y. Dong, *ACS Nano* **2015**, *9*, 4533.
[6] A. Sadhanala, S. Ahmad, B. Zhao, N. Giesbrecht, P. M. Pearce, F. Deschler, R. L. Hoye, K. C. Godel, T. Bein, P. Docampo, S. E. Dutton, M. F. De Volder, R. H. Friend, *Nano Lett.* **2015**, *15*, 6095.
[7] O. A. Jaramillo-Quintero, R. S. Sanchez, M. Rincon, I. Mora-Sero, *J. Phys. Chem. Lett.* **2015**, *6*, 1883.
[8] H. Cho, S. H. Jeong, M. H. Park, Y. H. Kim, C. Wolf, C. L. Lee, J. H. Heo, A. Sadhanala, N. Myoung, S. Yoo, S. H. Im, R. H. Friend, T. W. Lee, *Science* **2015**, *350*, 1222.
[9] T. Matsushima, F. Bencheikh, T. Komino, M. R. Leyden, A. S. D. Sandanayaka, C. Qin, C. Adachi, *Nature* **2019**, *572*, 502.
[10] X. Dai, Z. Zhang, Y. Jin, Y. Niu, H. Cao, X. Liang, L. Chen, J. Wang, X. Peng, *Nature* **2014**, *515*, 96.
[11] M. Stoppa, A. Chiolerio, *Sensors* **2014**, *14*, 11957.
[12] R. L. Hoye, M. R. Chua, K. P. Musselman, G. Li, M. L. Lai, Z. K. Tan, N. C. Greenham, J. L. MacManus-Driscoll, R. H. Friend, D. Credgington, *Adv. Mater.* **2015**, *27*, 1414.
[13] Z. Chen, C. Zhang, X. F. Jiang, M. Liu, R. Xia, T. Shi, D. Chen, Q. Xue, Y. J. Zhao, S. Su, H. L. Yip, Y. Cao, *Adv. Mater.* **2017**, 29.
[14] J. C. Yu, D. B. Kim, G. Baek, B. R. Lee, E. D. Jung, S. Lee, J. H. Chu, D. K. Lee, K. J. Choi, S. Cho, M. H. Song, *Adv. Mater.* **2015**, *27*, 3492.
[15] J. Wang, N. Wang, Y. Jin, J. Si, Z. K. Tan, H. Du, L. Cheng, X. Dai, S. Bai, H. He, Z. Ye, M. L. Lai, R. H. Friend, W. Huang, *Adv. Mater.* **2015**, *27*, 2311.
[16] Y. H. Kim, H. Cho, J. H. Heo, T. S. Kim, N. Myoung, C. L. Lee, S. H. Im, T. W. Lee, *Adv. Mater.* **2015**, *27*, 1248.
[17] J. Li, X. Shan, S. G. R. Bade, T. Geske, Q. Jiang, X. Yang, Z. Yu, *J. Phys. Chem. Lett.* **2016**, *7*, 4059.
[18] S. Y. Chou, R. Ma, Y. Li, F. Zhao, K. Tong, Z. Yu, Q. Pei, *ACS Nano* **2017**, *11*, 11368.
[19] D. K. Mohamad, J. Griffin, C. Bracher, A. T. Barrows, D. G. Lidzey, *Adv. Energy Mater.* **2016**, *6*, 1600994.
[20] J. E. Bishop, T. J. Routledge, D. G. Lidzey, *J. Phys. Chem. Lett.* **2018**, *9*, 1977.
[21] A. Liu, K. Liu, H. Zhou, H. Li, X. Qiu, Y. Yang, M. Liu, *Sci. Bull.* **2018**, *63*, 1591.
[22] Y. Zhong, R. Munir, J. Li, M.-C. Tang, M. R. Niazi, D.-M. Smilgies, K. Zhao, A. Amassian, *ACS Energy Lett.* **2018**, *3*, 1078.
[23] J. H. Kim, S. T. Williams, N. Cho, C.-C. Chueh, A. K. Y. Jen, *Adv. Energy Mater.* **2015**, *5*, 1401229.
[24] Y. Liu, F. Li, L. Qiu, K. Yang, Q. Li, X. Zheng, H. Hu, T. Guo, C. Wu, T. W. Kim, *ACS Nano* **2019**, *13*, 2042.
[25] L. Shi, L. Meng, F. Jiang, Y. Ge, F. Li, X. g. Wu, H. Zhong, *Adv. Funct. Mater.* **2019**, *29*, 1903648.
[26] J. Yu, M. Wang, S. Lin, *ACS Nano* **2016**, *10*, 11044.
[27] K. Walzer, B. Maennig, M. Pfeiffer, K. Leo, *Chem. Rev.* **2007**, *107*, 1233.
[28] M. Laurenti, D. Perrone, A. Verna, C. Pirri, A. Chiolerio, *Micromachines* **2015**, *6*, 1729.
[29] Z. Yu, X. Niu, Z. Liu, Q. Pei, *Adv. Mater.* **2011**, *23*, 3989.
[30] L. Cai, S. Zhang, Y. Zhang, J. Li, J. Miao, Q. Wang, Z. Yu, C. Wang, *Adv. Mater. Technol.* **2018**, *3*, 1700232.
[31] C.-Y. Chang, K.-T. Lee, W.-K. Huang, H.-Y. Siao, Y.-C. Chang, *Chem. Mater.* **2015**, *27*, 5122.
[32] M. Xie, H. Lu, L. Zhang, J. Wang, Q. Luo, J. Lin, L. Ba, H. Liu, W. Shen, L. Shi, C. Q. Ma, *Sol. RRL* **2018**, *2*, 1700184.
[33] F. Guo, H. Azimi, Y. Hou, T. Przybilla, M. Hu, C. Bronnbauer, S. Langner, E. Spiecker, K. Forberich, C. J. Brabec, *Nanoscale* **2015**, *7*, 1642.
[34] H. Lu, J. Lin, N. Wu, S. Nie, Q. Luo, C.-Q. Ma, Z. Cui, *Appl. Phys. Lett.* **2015**, *106*, 093302.

[35] Y. Zhou, C. Fuentes-Hernandez, J. Shim, J. Meyer, A. J. Giordano, H. Li, P. Winget, T. Papadopoulos, H. Cheun, J. Kim, *Science* **2012**, *336*, 327.
[36] X. Zhang, C. Sun, Y. Zhang, H. Wu, C. Ji, Y. Chuai, P. Wang, S. Wen, C. Zhang, W. W. Yu, *J. Phys. Chem. Lett.* **2016**, *7*, 4602.
[37] E. Saracco, B. Bouthinon, J. M. Verilhac, C. Celle, N. Chevalier, D. Mariolle, O. Dhez, J. P. Simonato, *Adv. Mater.* **2013**, *25*, 6534.
[38] H. Hu, R. G. Larson, *J. Phys. Chem. B* **2006**, *110*, 7090.
[39] A. Friederich, J. R. Binder, W. Bauer, B. Derby, *J. Am. Ceram. Soc.* **2013**, *96*, 2093.
[40] M. Cesarini, B. Brigante, M. Caironi, D. Natali, *ACS Appl. Mater. Interfaces* **2018**, *10*, 32380.
[41] L. W. Lo, J. Zhao, H. Wan, Y. Wang, S. Chakrabartty, C. Wang, *ACS Appl. Mater. Interfaces* **2021**, *13*, 21693.
[42] K. Mahmood, B. S. Swain, A. Amassian, *Adv. Energy Mater.* **2015**, *5*, 1500568.